iScience

CellPress
OPEN ACCESS

Article

A feasible interlayer strategy for simultaneous light and heat management in photothermal catalysis

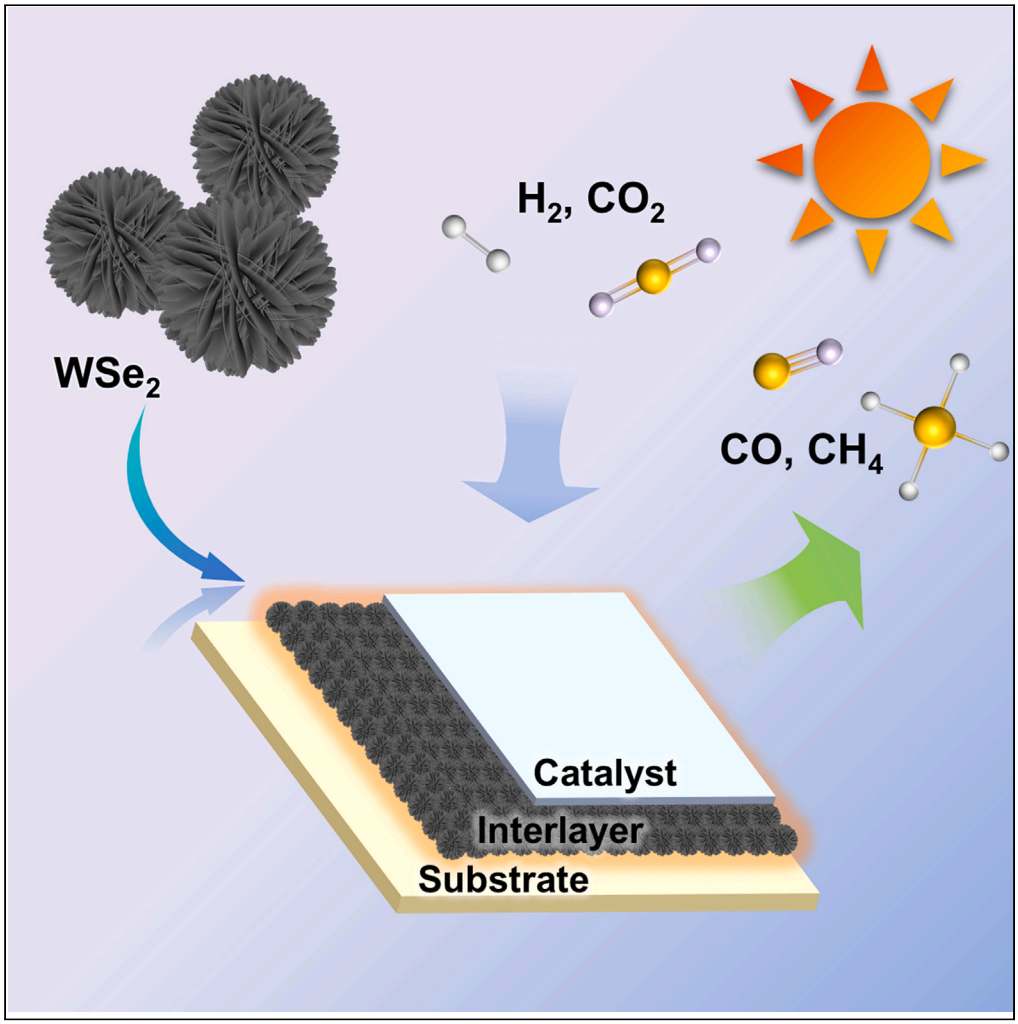

Yi Xiao, Kai Feng, Graham Dawson, Valeri P. Tolstoy, Xingda An, Chaoran Li, Le He

xdan@suda.edu.cn (X.A.)
crli@suda.edu.cn (C.L.)
lehe@suda.edu.cn (L.H.)

Highlights

A feasible and efficient WSe_2 interlayer-based photothermal conversion strategy

8-fold increase in CO_2 conversion rate by Ru/SiO_2-WSe_2-15

Raman characterizations of the photothermal performances

Xiao et al., iScience 27, 109792
June 21, 2024
https://doi.org/10.1016/j.isci.2024.109792

iScience

CellPress
OPEN ACCESS

Article

A feasible interlayer strategy for simultaneous light and heat management in photothermal catalysis

Yi Xiao,[1] Kai Feng,[1,2] Graham Dawson,[3] Valeri P. Tolstoy,[4] Xingda An,[1,2,*] Chaoran Li,[1,5,*] and Le He[1,2,6,*]

SUMMARY

Photothermal conversion represents one crucial approach for solar energy harvesting and its exploitation as a sustainable alternative to fossil fuels; however, an efficient, cost-effective, and generalized approach to enhance the photothermal conversion processes is still missing. Herein, we develop a feasible and efficient photothermal conversion strategy that achieves simultaneous light and heat management using supported metal clusters and WSe_2 interlayer toward enhanced CO_2 hydrogenation photothermal catalysis. The interlayer can simultaneously reduce heat loss in the catalytic layer and improve light absorption, leading to an 8-fold higher CO_2 conversion rate than the controls. The optical and thermal performance of WSe_2 interlayered catalysts on different substrates was quantified using Raman spectroscopy. This work demonstrates a feasible and generalized approach for effective light and heat management in solar harvesting. It also provides important design guidelines for efficient photothermal converters that facilitate the remediation of the energy and environmental crises faced by humans.

INTRODUCTION

The recent decades have seen the increasing exploitation of solar energy as an abundant, clean, and renewable alternative to traditional fossil energy that can significantly reduce energy consumption while achieving higher energy conversion efficiency.[1–7] Photothermal catalysis represents one significant approach of sunlight utilization that effectively converts it to thermal and eventually chemical energy.[8–16] Photothermal catalysis generally contains two integrated processes, namely photothermal conversion and surface catalytic reactions. In a typical photothermal catalytic pathway, the absorption of irradiation power first leads to production of charge carriers; through subsequent electron-electron (e^--e^-) and electron-phonon (e^--ph) scattering,[17–20] the kinetic energy of the charge carriers could be transformed into vibrational energy of the lattice and thus into heat.[21–25] The accumulated heat is able to increase the temperature on the catalyst surface in a highly localized manner, thereby thermodynamically initiating the reaction process.

Modulation of the light-to-heat conversion efficiency provides a generalized strategy to increase the solar harvesting and conversion efficiencies.[26,27] In this area, previous research efforts have primarily focused on two major approaches, through either light management or heat management.[26,28,29] For the former, intricately designed nanostructures have been reported that possess intense and broad absorption range in the sunlight spectrum, or that sustains distinct light modulation effects. For instance, nanoarray structures have been used to increase the light path during light propagation;[30,31] hollow structures have also been designed for light management through Mie scattering;[32] plasmonic superstructures have been proven to broaden the spectrum of light absorption via hybridization effect.[17,28,33] However, these methods typically require complex synthesis procedures, which results in limited applicability. On the other hand, heat management approaches aim at reducing the conductive, convective, and radiative heat losses in photothermal conversion due to the huge temperature difference between the catalyst and the surrounding environment.[34–36] Our group has recently proposed the nano-greenhouse effect, using mesoporous SiO_2 shells to act as a greenhouse gas-like effect that reduces heat dissipation by thermal radiation from the catalytic center.[36] Despite the efficacy of this approach, challenges still exist including limitations on the structure, composition, and intrinsic properties of the catalyst. Therefore, an efficient, cost-effective, and generalized approach for enhancement of the photothermal conversion processes in photothermal catalysis is still missing.

In this work, we have designed a generalized and efficient photothermal conversion strategy that achieves simultaneous light and heat management through a feasible interlayer approach. WSe_2, which possesses excellent thermal resistance,[37,38] is used as a thermal barrier

[1]Institute of Functional Nano & Soft Materials (FUNSOM), Soochow University, Suzhou 215123, China
[2]Jiangsu Key Laboratory of Advanced Negative Carbon Technologies, Soochow University, Suzhou, Jiangsu 215123, P.R. China
[3]Department of Chemistry, Xi'an Jiaotong Liverpool University, Suzhou, Jiangsu 215123, P.R. China
[4]Institute of Chemistry, Saint-Petersburg State University, St. Petersburg 199034, Russia
[5]Jiangsu Key Laboratory for Carbon-Based Functional Materials & Devices, Soochow University, Suzhou, Jiangsu 215123, P.R. China
[6]Lead contact
*Correspondence: xdan@suda.edu.cn (X.A.), crli@suda.edu.cn (C.L.), lehe@suda.edu.cn (L.H.)
https://doi.org/10.1016/j.isci.2024.109792

interlayer to reduce the heat loss from the catalytic layer composed of Ru/SiO_2 clusters, while improving the light absorption and the photothermal temperature of the active component. Raman spectroscopy was utilized as a quantitative approach to calibrate the photothermal conversion effect of the thermal barrier interlayer on various types of substrates. The simultaneous improvement of photothermal CO_2 conversion rate and CO selectivity was observed for photothermal catalysis in CO_2 hydrogenation reaction, where the reaction activity and CO selectivity are further investigated as a function of interlayer thickness and substrate type. This work demonstrates a feasible, generalized, and easily scalable approach for efficient light and heat management in solar harvesting applications. Under a broader context, it provides important design guidelines for efficient photothermal catalysts, and is likely to contribute to alleviating the energy and environmental crises faced by humans.

RESULTS AND DISCUSSION

Design and characterization of the Ru/SiO_2 catalyst supported by WSe_2 interlayer

Simultaneous light and heat management in photothermal catalytic materials is highly desired yet challenging, particularly for supported powder catalysts, which is a predominant form of typical photothermal catalysts due to their large specific surface area and space utilization efficacy.[39–41] However, reconciling the need to simultaneously improve light absorption and catalytic properties often presents conflicting demands in material design.[42] For example, the catalytic performance of large metal particles with high light absorption tends to be poor, while small metal particles with high catalytic performance have limited light absorption capability.[43] Moreover, the direct contact mode between the catalyst layer and the substrate facilitates a continuous transfer of generated heat to the substrate layer.[28,34] As a result, higher demands are placed on the thermal insulation properties of the substrate materials.

To address these issues, an interlayer was introduced to substrate-supported catalysts to form a catalyst-interlayer-substrate configuration. An ideal interlayer should possess excellent light-absorption ability that boosts the light-to-heat conversion of the system, while also exhibiting desirable heat preservation capability to minimize heat loss and enhance energy conversion efficiency. Meanwhile, to guarantee the general applicability of the interlayer, stability of the interlayer at elevated temperatures is also an important consideration. WSe_2 has been reported to possess very low thermal conductivity (0.05 W $m^{-1}\cdot K^{-1}$)[37] as well as a narrow band gap of 1.6 eV,[44–46] which renders it a suitable proof-of-concept material to implement the light and heat management strategy as an interlayer (Figure 1A). Self-supported flower structures of WSe_2 were used, as this unique structure ensures a more porous and fluffy morphology, allowing for increased gas retention, and consequently reducing heat transfer.[47] X-ray diffraction (XRD) pattern in Figure 1B reveals that diffraction peaks can be well-indexed as hexagonal tungsten diselenide (JCPDS No. 87–2418), with the (002), (100), and (103) planes observed at angles of 13.6°, 31.4°, and 37.8°, respectively. Transmission electron microscopy (TEM) image of the as-prepared WSe_2 confirms the flower-petaloid-like architecture with an approximate diameter of 1.5 μm (Figure 1C). The petal was composed of few-layered/monolayered WSe_2 nanosheets (Figure S1). Notably, the multiple refraction and scattering occurring within the flower-like structure can enhance the interaction between light and material, which implies this structure may further improve the efficiency of light utilization. High-resolution TEM (HRTEM) image clearly depicts the measured lattice spacing as d = 0.67 nm (Figure 1D), which is consistent with the calculated value of 13.6° from the XRD pattern using the Bragg equation, indicating that it corresponds to the (002) planes of WSe_2.[48] Energy-dispersive spectroscopy (EDS) elemental mapping (Figure 1E) demonstrate a complete overlap in the distribution of W and Se, further indicating the formation of WSe_2 compound. To further confirm the composition of WSe_2, Raman spectroscopy was next used, which displays clear vibrational modes of WSe_2 at 249 cm^{-1} and 258 cm^{-1}, corresponding to the E^1_{2g} (in-plane) and A_{1g} modes, respectively (Figure S2).[48,49]

In terms of catalyst composition in the catalysts-interlayer-substrate model, Ru clusters supported on SiO_2 substrates (Ru/SiO_2) was used. Supported metal cluster catalysts (SMCs) have aroused increasing research interest due to their unique geometric and electronic structures as well as abundant surface active sites.[12,20,50–56] In particular, Ru/SiO_2 SMCs have been shown to possess good intrinsic CO_2 hydrogenation reactivity.[43,57] However, the low light absorption capability of the Ru clusters and the high the thermal conductivity of the substrate limit the photothermal conversion efficiency, which further affects the subsequent photothermal catalytic activity. Ru/SiO_2 SMCs thus represents desirable test platforms for the interlayer strategy. Ru/SiO_2 was prepared by impregnation. The average size of Ru, obtained from HRTEM, was found to be 1.5 ± 0.5 nm, which is within the cluster range (Figure S3). EDS mapping images further evidenced a uniform distribution of Ru clusters on the support (Figure S3C). The absence of characteristic peaks corresponding to metallic Ru in the XRD pattern of Ru/SiO_2 can be attributed to the low content of Ru (2.1 wt %) as confirmed by ICP-MS (inductively coupled plasma mass spectrometry) (Figure S4).[58]

A layered structure consisting of Ru catalyst/WSe_2 interlayer/substrate, was assembled by layer-by-layer drop casting onto glass fiber substrates and no significant electrostatic interaction between different layers could be present (Table S1). The thickness of the interlayer was controlled by adjusting the amount of WSe_2. To determine the thicknesses of the interlayer, scanning electron microscopy (SEM) was used for cross-sectional characterization. The control sample depicted in Figure 1F displayed a dual-layer structure in the absence of WSe_2. Thicknesses of 15 μm, 26 μm, and 39 μm were obtained corresponding to the addition amounts of WSe_2 at 5 mg, 10 mg, and 15 mg (Figures 1G–1I), respectively denoted as Ru/SiO_2-WSe_2-5, Ru/SiO_2-WSe_2-10, and Ru/SiO_2-WSe_2-15. The thickness and mass of introduced WSe_2 exhibits a linear relationship (Figure S5). The hierarchical structure can be clearly observed in the EDS diagram, where Ru/SiO_2, WSe_2, and the substrate material are identified in order from top to bottom. (Figure S6).

Enhanced light management by the interlayer strategy

To provide direct evidence on the enhancement in light management by the interlayer strategy, the absorbance properties of the catalysts were first probed. The optical images of these four samples clearly illustrate the transition in color from light gray to black upon the

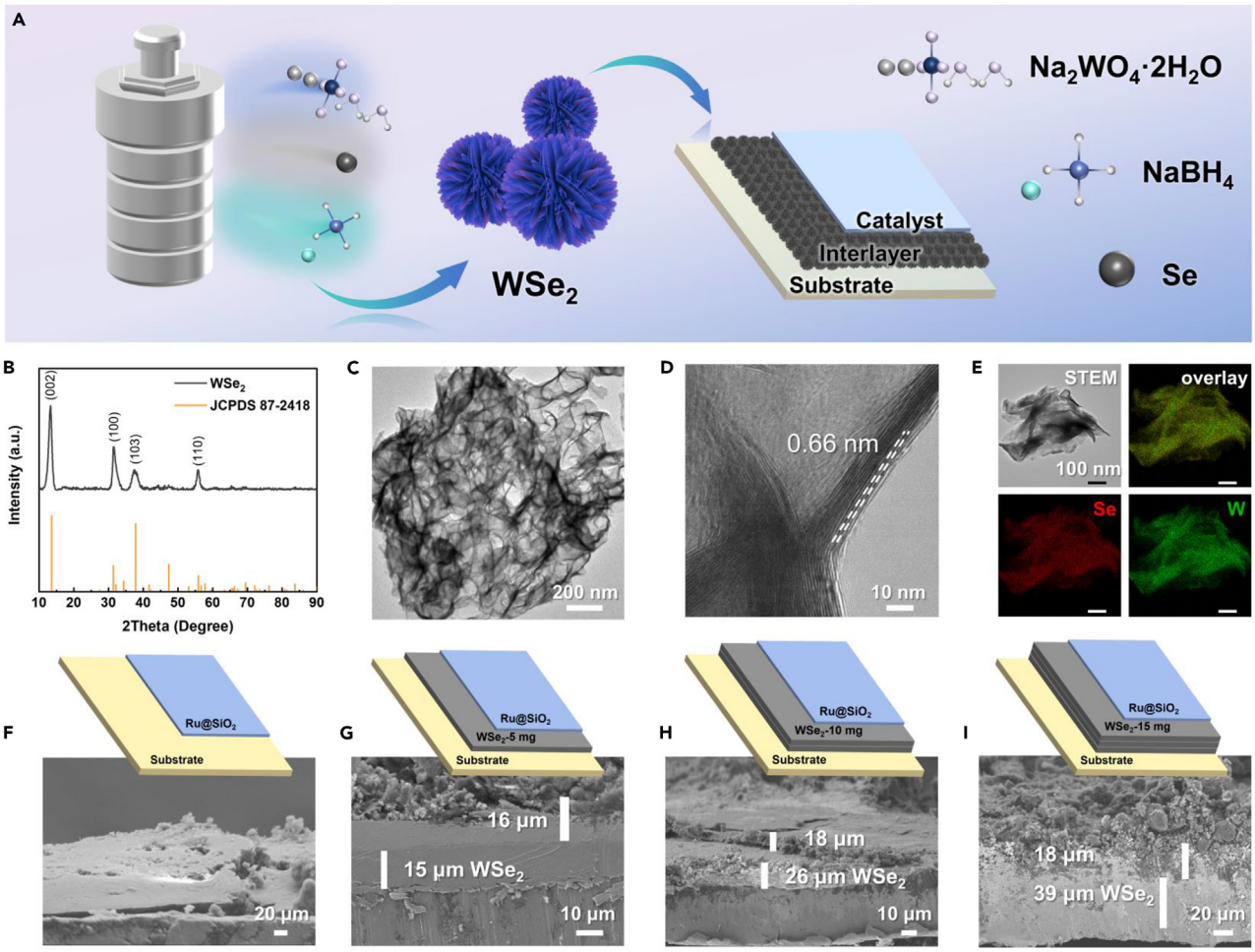

Figure 1. Scheme and structural characterizations of WSe_2 interlayered Ru catalysts

(A) Schematic illustration of the fabrication process of WSe_2 and serving as the interlayer.

(B) XRD pattern of WSe_2 (black) in comparison with the reference of WSe_2 (orange).

(C and D) (C) TEM image and (D) HRTEM image of WSe_2.

(E) EDS mappings of WSe_2.

(F–I) Schematic and the cross-sectional SEM images of (F) Ru/SiO_2, (G) Ru/SiO_2-WSe_2-5, (H) Ru/SiO_2-WSe_2-10, and (I) Ru/SiO_2-WSe_2-15.

introduction of WSe_2 interlayers (Figures 2A–2D). The light absorption capability of the catalysts was evaluated using UV-vis-NIR diffuse reflectance spectroscopy (DRS). The introduction of the WSe_2 interlayer leads to a significant enhancement in light absorption, as compared to the Ru/SiO_2 control (Figure 2E). In particular, the absorption in the near-infrared region has increased significantly from 30% to 80%. This is especially helpful for solar energy harvesting and light-to-heat conversion, as near infrared (NIR) accounts for a large portion of the solar spectrum, and that NIR irradiation can more effectively couple to the vibrational frequencies of solid materials for heat generation.[59,60] Meanwhile, with the increase in the thickness of the WSe_2 layer, there was no significant difference observed in the light absorption performance among the samples, suggesting that a 15-μm layer of WSe_2 is sufficient for light absorption. These results demonstrate the remarkable improvement of light utilization through the implementation of a WSe_2 interlayer.

Enhanced heat management by the interlayer strategy

To evidence the efficacy of the interlayer strategy in improving the heat management capability of the catalysts through reducing heat dissipation, a series of characterizations were performed. Infrared camera was first used to measure the surface temperature of different samples under identical illumination conditions. Figure 3A illustrates that under Xenon lamp irradiation at 2.9 W/cm^2, the maximum surface temperature of Ru/SiO_2 reaches approximately 326°C. By introducing 5 mg WSe_2, the temperature experienced a substantial increase of nearly 50°C, reaching 376°C (Figure 3B). This notable rise can be attributed to the synergistic effect resulting from the enhanced light absorption capability and exceptional thermal insulation performance exhibited by WSe_2. A further increase in the surface temperature was observed with increase

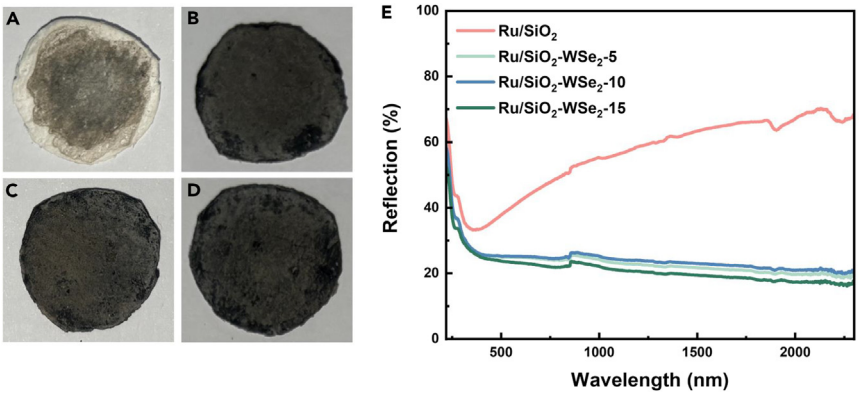

Figure 2. Light absorption ability of WSe_2 interlayered Ru catalysts

(A–D) Digital photos of (A) Ru/SiO_2, (B) Ru/SiO_2-WSe_2-5, (C) Ru/SiO_2-WSe_2-10, and (D) Ru/SiO_2-WSe_2-15.

(E) DRS of these four samples.

in the thickness of the WSe_2 layer. The introduce of 10 mg layer of WSe_2 elevated the temperature of Ru/SiO_2 to 387°C, whereas the Ru/SiO_2-WSe_2-15 sample achieved a maximum surface temperature of 395°C (Figures 3C and 3D). A linear relationship can be obtained between the increase in surface temperature and the thickness of the WSe_2 layer, and the slope was approximately 1°C/μm. Moreover, analysis of the time-dependent temperature revealed that pure Ru/SiO_2 control reached a plateau after more than 10 s. In contrast, the WSe_2 interlayered samples achieved to equilibrium temperature in just 5 s (Figure 3E). The higher light-to-heat conversion efficiency of supported catalysts-interlayer accelerates the increase in temperature on the catalyst surface upon illumination. Besides, in order to prove the efficacy of the nanoflower morphology in facilitating microscale heat preservation of the interlayer, bulk WSe_2 has also been used to prepare comparison samples (Figure S7). Comparing Figures 3A–3D, the addition of bulk WSe_2 also leads to an increase in the surface temperature of Ru/SiO_2, but the enhancement is not as much as that of WSe_2 with nanoflower morphology.

Considering the comparable light absorption exhibited by WSe_2 interlayered samples in Figure 2 and their similar light-to-heat conversion abilities, the additional temperature increase observed in Ru/SiO_2-WSe_2-10 and Ru/SiO_2-WSe_2-15 compared to Ru/SiO_2-WSe_2-5 can primarily be attributed to the heat management contribution. With an increase in the WSe_2 thickness, there is a decrease in its ability to transfer heat to the substrate, which highlights the impressive heat management capabilities of interlayer materials. To evidence this hypothesis and to decouple light absorption and heat management in the measurements, Ru/SiO_2 and Ru/SiO_2-WSe_2-5 were illuminated under different light intensities to reach the same temperature of 325°C. After that, illumination was cut off and the systems cooled to room temperature, and their cooling curves were measured and assessed by IR cameras. Importantly, the introduction of WSe_2 significantly improved the cooling time from 6 s to 13 s (Figure 3F). This directly corroborates the high thermal insulation performance of WSe_2, which provides better insulation and further demonstrates the excellent heat management performance of our strategy.

Raman temperature calibration measurements

In order to further probe and quantify the efficacy of the interlayer strategy on photothermal conversion, Raman spectroscopy was next utilized to calibrate the surface temperatures of Ru/SiO_2 and Ru/SiO_2-WSe_2-5 on glassy fiber substrates. Since the temperature obtained by the infrared camera is the macroscopic temperature of the sample surface, the Raman measurements are more likely to reflect the actual microscopic temperatures on the surface of the active components. It has been reported that the Raman scattering intensity would increase significantly as the illumination time on catalyst surface increases, as the intensity of the lattice vibrational modes is proportional to temperature.[61,62] Therefore, it is anticipated that larger Raman peak intensities are associated with higher local temperatures, and that the slopes of the irradiation time-Raman scattering intensity plots are associated with the rate of heating under different illumination conditions.

To first probe the intrinsic characteristic peaks of WSe_2 and Ru/SiO_2, Raman spectra were first obtained for Ru/SiO_2-WSe_2-5 at room temperature without external heating or illumination other than the Raman laser (Figure 4A). The peak at 249 cm^{-1} belongs to the characteristic peaks of W-Se, while the peaks centered 592 cm^{-1}, 661 cm^{-1}, and 755 cm^{-1} belong to the E_g, A_{1g}, and B_{2g} of Ru-O, respectively.[63] A slight shift of the Ru-O peaks toward high frequencies is observed, which could be due to Se-induced changes in the chemical environment.[64] Afterward, white light illumination with a light power of 0.1 and 0.3 W/cm^2 are applied to the samples for different irradiation times, in order to probe the effect of photothermal conversion. As expected, an enhancement of the peak intensity of the Ru-O bond occurred with increasing illumination time due to the temperature increase of the active component (Figures 4A and S8). The relationship between peak intensity and light duration was next fitted, and an evident linear relationship was observed (Figures 4B and 4C). In addition, the peak intensity of Ru-O also showed a continuous rise with increasing light intensities (Figures 4D, S9, and S10; Table S2). An identical trend is also observed for pure Ru/SiO_2, with the Raman peak intensity of 0.3 W/cm^2 significantly higher than that of 0.1 W/cm^2 after the same time of illumination (Figures 4E and S11). A linear fit was performed to the maximum Raman intensity and light application time,

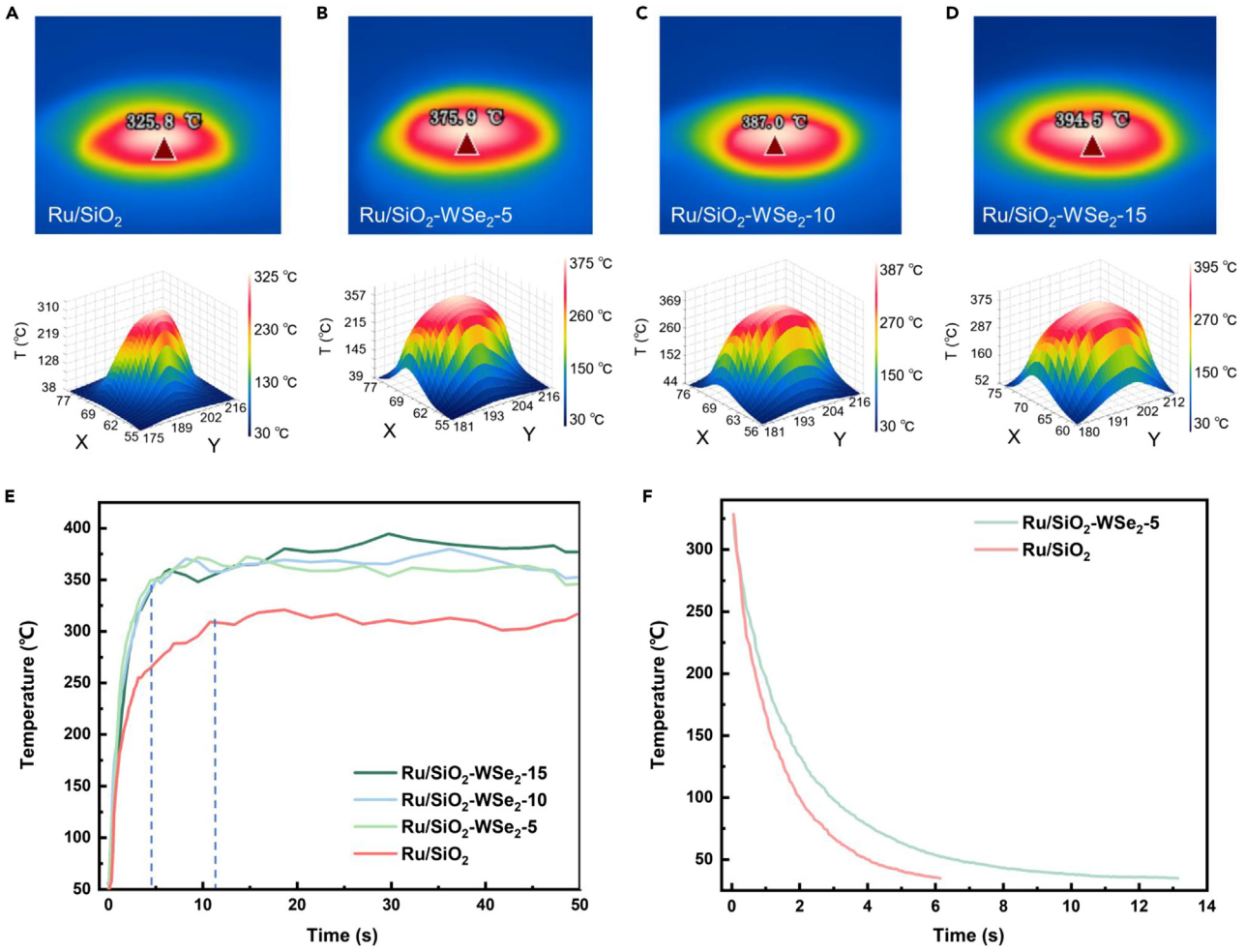

Figure 3. Infrared camera images of catalyst films

(A–D) Infrared camera images and 3D plots of (A) Ru/SiO_2, (B) Ru/SiO_2-WSe_2-5, (C) Ru/SiO_2-WSe_2-10, and (D) Ru/SiO_2-WSe_2-15 upon Xenon lamp irradiation at 2.9 W/cm^2.

(E) Time-dependent surface temperature profiles of heating on different catalyst films.

(F) Time-dependent surface temperature profiles of the cooling curves of Ru/SiO_2 and Ru/SiO_2-WSe_2-5 from 325°C.

revealing that the slope of the trend line under 0.3 W/cm^2 (y = 150.06x+2146.65) is significantly higher compared to the fitted trend line under 0.1 W/cm^2 (y = 79.08x+1594.74) (Figures 4F and 4G). This is consistent with our anticipation, and indicates that the rate of temperature increase is faster at higher light intensities.

In order to explore the impact of WSe_2 on the rate of microscale temperature elevation of active components and to evidence the efficacy of our insulating interlayer strategy, the local temperature calibrated by Raman spectroscopy and heating rates were compared for the purpose of contrasting the effect of the WSe_2 interlayer on the rate of heat-up. Importantly, for the peak intensity vs. time fitting trend of the Ru-O bond under 0.3 W/cm^2, the linear slope was found to be elevated significantly after the addition of WSe_2 (y = 273.78x+2533.64) compared to without WSe_2 insulating interlayer (y = 150.06x+2146.65). This is consistent with the previous case without WSe_2, and implies that the addition of WSe_2 can substantially enhance the rate of temperature increase in Ru. This effect is attributed to the synergistic effect between optical and thermal management enabled by the interlayer strategy.

To assess the reliability of the calibration by Raman spectroscopy, the Raman intensities for different light intensities and irradiation times were plotted against the temperatures captured by the infrared camera under identical illumination conditions (Figure 4H). Almost identical temperatures were calculated from the fitted linear equation compared for calibration curves obtained with different illumination times (Tables S3 and S4). This demonstrates the high reliability of the temperature measurement method. In addition to the IR camera, the Ru-O peak intensity was also calibrated with a heated plate (Figure S12). It was found that the temperatures calculated from this calibration line were generally higher than those measured by the IR camera (Table S5). This may be explained by the fact that the IR camera tests the macroscopic peripheral temperatures, whereas the Raman tests the peripheral temperatures of the active components.

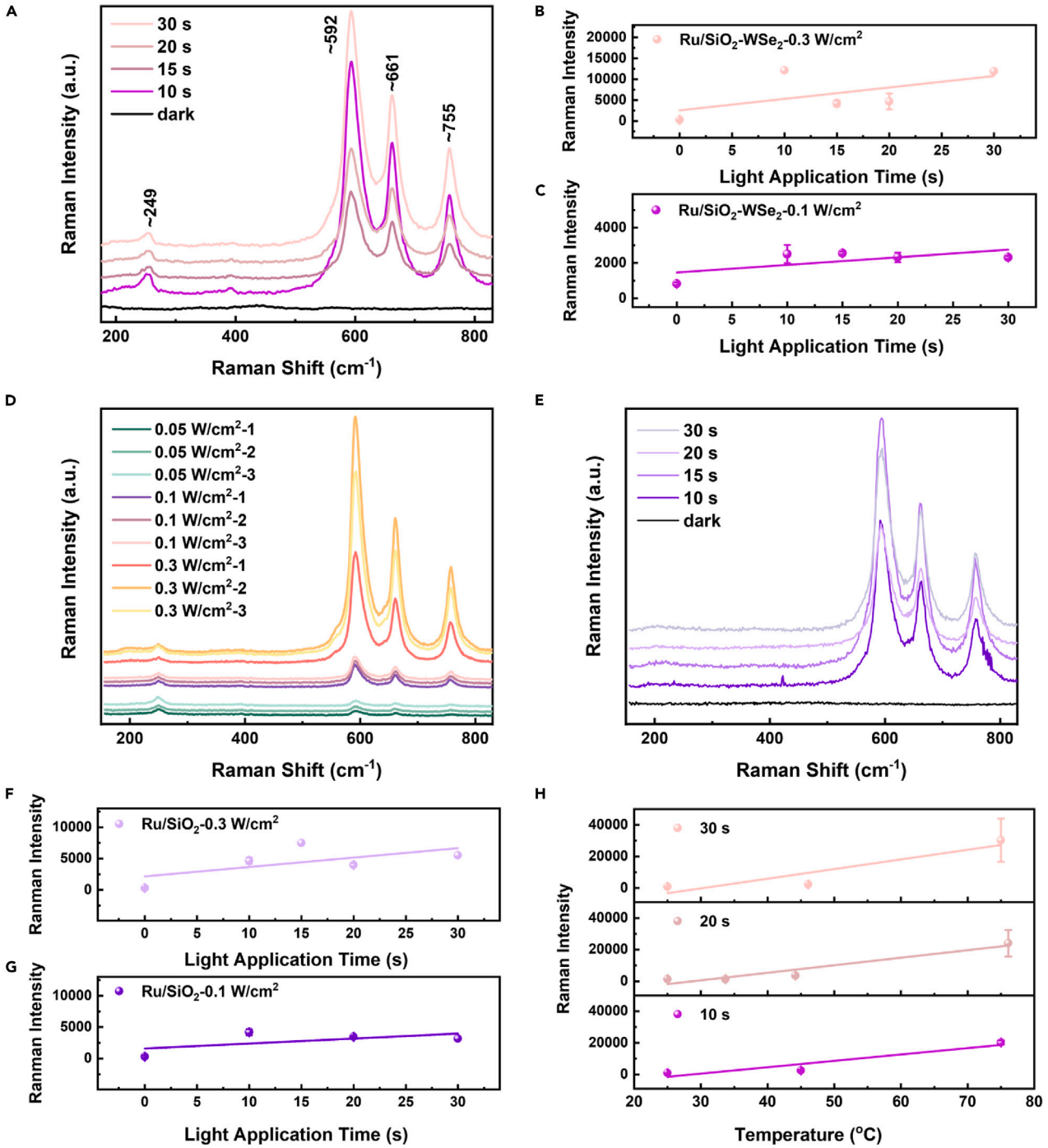

Figure 4. Raman spectrum and peak intensity-time fitting trend of the Ru-O bond of ~592 cm^{-1}

(A) Raman spectrum of Ru/SiO_2-WSe_2-5 after different irradiation time at 0.3 W/cm^2.

(B and C) Linear fitting of Ru-O Raman peaks after irradiation with the same light intensities for the different light application time for Ru/SiO_2-WSe_2-5 of (B) 0.3 W/cm^2 and (C) 0.1 W/cm^2.

(D) Raman spectrum of Ru/SiO_2 after different light intensity of 20 s.

(E) Raman spectrum of Ru/SiO_2 after different irradiation time at 0.3 W/cm^2.

(F and G) Linear fitting of Ru-O Raman peaks after irradiation with the same light intensities for the different light application time for Ru/SiO_2-5 of (F) 0.3 W/cm^2 and (G) 0.1 W/cm^2.

(H) Linear fitting of Ru-O Raman peaks after irradiation with different light intensities for the same irradiation time, and the temperature is measured by an infrared camera.

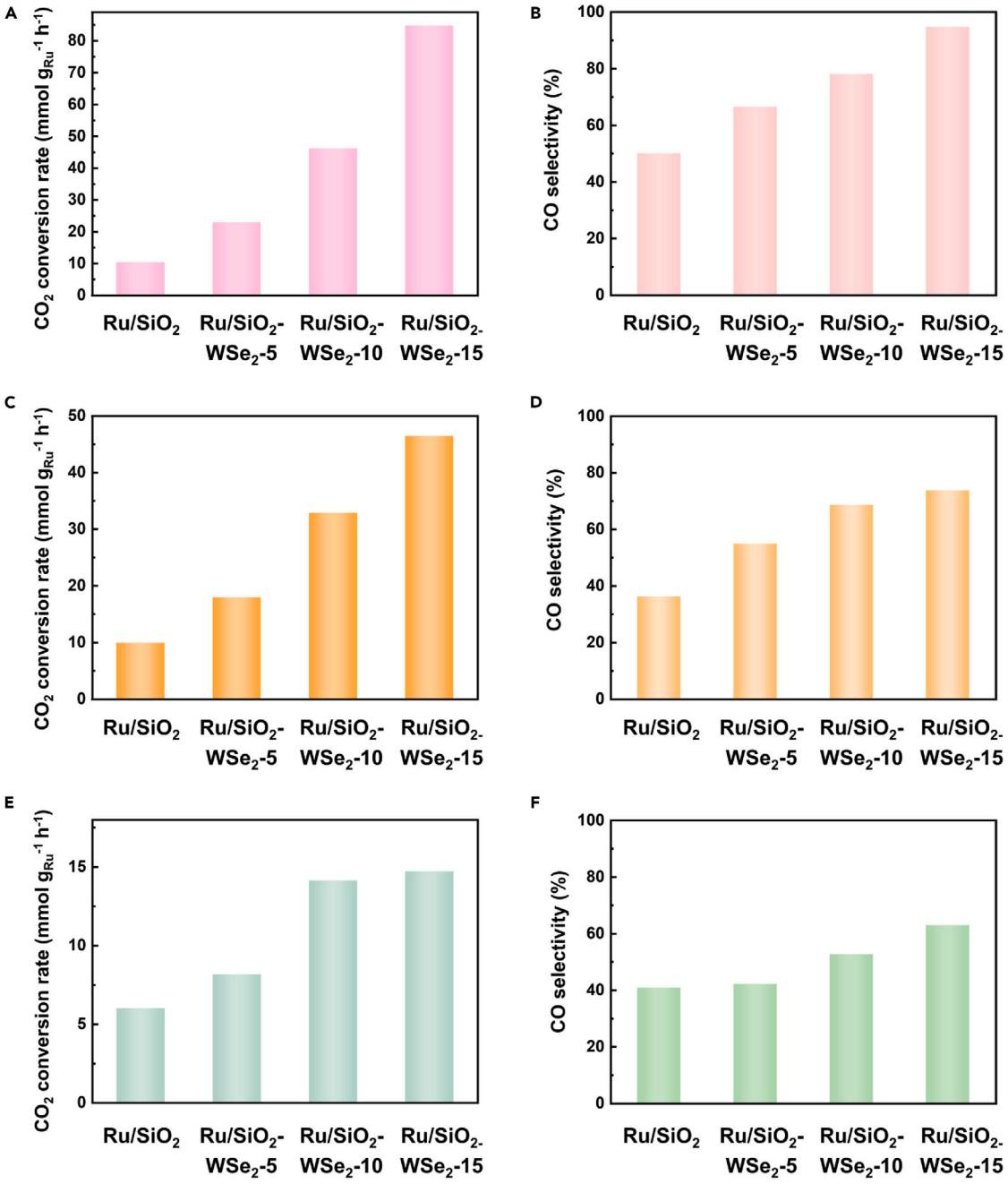

Figure 5. Photothermal catalytic performance

(A–F) Photothermal catalytic activity and CO selectivity on (A and B) glass fiber substrates, (C and D) Cu substrate, and (E and F) Si substrate.

Applicability of the interlayer strategy in photothermal catalysis

The incorporation of the WSe_2 interlayer in Ru/SiO_2-WSe_2 significantly enhances the light absorption and photothermal conversion efficiency, thereby establishing a solid foundation for enhancing their photothermal catalytic performance. Photothermal CO_2 hydrogenation was selected as a model reaction to demonstrate the application of the interlayer strategy (Figures 5A and 5B). The reaction was driven by a xenon lamp simulating sunlight without external heating (Figure S13). CO and CH_4 were the only detected products for all samples, suggesting that the reverse water gas shift (RWGS) and Sabatier reactions were triggered. With the concentrated light of 2.9 W/cm^2, Ru/SiO_2-WSe_2-5 exhibited double the CO_2 conversion rate than Ru/SiO_2 (after normalization by metal loading). This was attributed to the higher local temperature resulting from the excellent thermal insulation performance and enhanced light absorption capability of the WSe_2 layer, which can

be referred to as the combined action of light and heat management. Moreover, with the increase in the amount of the WSe_2 interlayer, further improvements in CO_2 conversion rate and CO selectivity were observed. As was demonstrated in the previous sections, increasing the thickness of the WSe_2 interlayer does not result in improved light absorption performance. Thus, this enhancement of activity is more likely ascribed to increases in local temperatures and further enhancement in heat management. The RWGS reaction is characterized as an endothermic process, where a higher temperature thermodynamically enhances the propensity for the formation of the reaction product CO, which was consistent with the observed increase in CO selectivity associated with increasing WSe_2 layer thickness.[65]

The interlayer strategy exhibits high versatility and scalability, enabling easy extension of the proposed method to diverse substrates. Copper (Cu) sheet and silicon (Si) slice were utilized as substrates to further validate the generalization of the interlayer strategy. The DRS curves of the samples on Cu sheet and Si slice show similar trends to those on the glass fiber substrates, indicating that the introduction of WSe_2 significantly enhances the light absorbance performance (Figure S14). It was also found that the presence of the WSe_2 layer led to an increase in surface temperature, while increasing the thickness of the insulation layer further improves its photothermal conversion capability (Figure S15). Compared to the controls, the Ru/SiO_2 catalyst sustains a uniform heat distribution, whereas the insulating WSe_2 layer displays clear gradients in temperature, resulting in the low temperature in the bottom substrate layer (Figure S16). After natural cooling under air conditions for 1 μs, the simulation indicates that the WSe_2 interlayer effectively slows down the cooling rate of the system (Figure S17). To probe the generalized effect of our interlayer strategy on the photothermal conversion efficacy on different substrate types, the Raman temperature calibration measurements were also performed on Si and Cu substrates. In general, similar results to those of glass fiber substrates were observed in Raman tests using different substrates (Figure S18), where a proportionally higher Raman scattering intensity is observed as the illumination power and irradiation time increased. Based on the aforementioned characterizations, it could be concluded that the insulation layer strategy not only provides a practical temperature increase in the micro-level of the active component, but is also widely applicable, laying the groundwork for its scalable utilization in potential large-scale sunlight harvesting or catalytic applications.

As a result, the photothermal catalytic reactivity and CO selectivity were enhanced (Figures 5C–5F). It is worth noting that the enhancement of photothermal conversion capacity and RWGS reactivity is not only limited to the same substrate, but also compensates for the difference in thermal conductivity of different substrates. Since the thermal conductivity of Si is higher than that of Cu, the temperature of pure Ru/SiO_2 on Si slice is lower than Cu sheet (194°C < 213°C), which results in a lower catalytic activity. However, the addition of the interlayer has overcome the inferior heat preservation effect of the silicon substrate, leading to a higher catalytic performance.

Conclusion

In conclusion, through a feasible and effective interlayer strategy, we have achieved simultaneous light and heat management in a prototypical Ru/SiO_2 SMC toward enhanced photothermal catalysis of CO_2 hydrogenation. The utilization of an interlayer with desirable light absorption and thermal insulating capabilities effectively increased the solar energy harvesting and light-to-heat conversion efficiencies, as evidenced from both infrared camera and Raman spectroscopy measurements. Our strategy provides generalized insights into the design principles of an efficient photothermal converter and catalyst. In addition, the feasible interlayer approach is easily scalable, which presents intriguing potentials for large-scale industrial applications as well as great promises for ameliorating the energy structure and environmental issues.

Limitations of the study

Our strategy is effective in terms of performance enhancement for catalysts with excellent intrinsic catalytic performance and weak light absorption. However, for catalysts with inherently better light absorption, the strategy may provide improvements mainly in thermal management, while the enhancement in light management may be more limited.

STAR★METHODS

Detailed methods are provided in the online version of this paper and include the following:

- KEY RESOURCES TABLE
- RESOURCE AVAILABILITY
  - Lead contact
  - Materials availability
  - Data and code availability
- METHOD DETAILS
  - Materials
  - Synthesis of WSe_2 powders
  - Synthesis of Ru/SiO_2 catalysts
  - Characterizations
  - Photocatalytic testing

SUPPLEMENTAL INFORMATION

Supplemental information can be found online at https://doi.org/10.1016/j.isci.2024.109792.

ACKNOWLEDGMENTS

We acknowledge the support from the National Key R&D Program of China (2021YFF0502000), National Natural Science Foundation of China (52172221, 52272229, 22302137, and 51920105005), Jiangsu Key Laboratory for Carbon-Based Functional Materials and Devices (ZZ2201), Suzhou Key Laboratory of Functional Nano & Soft Materials, and Collaborative Innovation Center of Suzhou Nano Science and Technology.

AUTHOR CONTRIBUTIONS

Conceptualization, L.H.; resources, L.H., C.L., and X.A.; investigation, Y.X.; formal analysis, K.F. and G.D.; writing – original draft, Y.X.; writing – review & editing, V.P.T., C.L., and X.A.; supervision, L.H.

DECLARATION OF INTERESTS

The authors declare no competing interests.

Received: December 23, 2023
Revised: March 25, 2024
Accepted: April 17, 2024
Published: April 26, 2024

REFERENCES

1. Inoue, T., Fujishima, A., Konishi, S., and Honda, K. (1979). Photoelectrocatalytic reduction of carbon-dioxide in aqueous suspensions of semiconductor powders. Nature *277*, 637–638. https://doi.org/10.1038/277637a0.
2. Zhou, P., Navid, I.A., Ma, Y., Xiao, Y., Wang, P., Ye, Z., Zhou, B., Sun, K., and Mi, Z. (2023). Solar-to-hydrogen efficiency of more than 9% in photocatalytic water splitting. Nature *613*, 66–70. https://doi.org/10.1038/s41586-022-05399-1.
3. Aslam, U., Rao, V.G., Chavez, S., and Linic, S. (2018). Catalytic conversion of solar to chemical energy on plasmonic metal nanostructures. Nat. Catal. *1*, 656–665. https://doi.org/10.1038/s41929-018-0138-x.
4. Lu, Z., Xu, Y., Zhang, Z., Sun, J., Ding, X., Sun, W., Tu, W., Zhou, Y., Yao, Y., Ozin, G.A., et al. (2023). Wettability engineering of solar methanol synthesis. J. Am. Chem. Soc. *145*, 26052–26060. https://doi.org/10.1021/jacs.3c07349.
5. Zhao, X., He, D., Xia, B.Y., Sun, Y., and You, B. (2023). Ambient electrosynthesis toward single-atom sites for electrocatalytic green hydrogen cycling. Adv. Mater. *35*, 2210703. https://doi.org/10.1002/adma.202210703.
6. Zhao, X., Du, L., You, B., and Sun, Y. (2020). Integrated design for electrocatalytic carbon dioxide reduction. Catal. Sci. Technol. *10*, 2711–2720. https://doi.org/10.1039/D0CY00453G.
7. Zhao, J., Liu, J., Li, Z., Wang, K., Shi, R., Wang, P., Wang, Q., Waterhouse, G.I.N., Wen, X., and Zhang, T. (2023). Ruthenium-cobalt single atom alloy for CO photo-hydrogenation to liquid fuels at ambient pressures. Nat. Commun. *14*, 1909. https://doi.org/10.1038/s41467-023-37631-5.
8. Jiang, H., Wang, L., Kaneko, H., Gu, R., Su, G., Li, L., Zhang, J., Song, H., Zhu, F., Yamaguchi, A., et al. (2023). Light-driven CO_2 methanation over Au-grafted $Ce_{0.95}Ru_{0.05}O_2$ solid-solution catalysts with activities approaching the thermodynamic limit. Nat. Catal. *6*, 519–530. https://doi.org/10.1038/s41929-023-00970-z.
9. Zhou, S., Shang, L., Zhao, Y., Shi, R., Waterhouse, G.I.N., Huang, Y.C., Zheng, L., and Zhang, T. (2019). Pd single-atom catalysts on nitrogen-doped graphene for the highly selective photothermal hydrogenation of acetylene to ethylene. Adv. Mater. *31*, e1900509. https://doi.org/10.1002/adma.201900509.
10. Meng, X., Liu, L., Ouyang, S., Xu, H., Wang, D., Zhao, N., and Ye, J. (2016). Nanometals for solar-to-chemical energy conversion: From semiconductor-based photocatalysis to plasmon-mediated photocatalysis and photo-thermocatalysis. Adv. Mater. *28*, 6781–6803. https://doi.org/10.1002/adma.201600305.
11. Zhang, Z., Mao, C., Meira, D.M., Duchesne, P.N., Tountas, A.A., Li, Z., Qiu, C., Tang, S., Song, R., Ding, X., et al. (2022). New black indium oxide-tandem photothermal CO_2-H_2 methanol selective catalyst. Nat. Commun. *13*, 1512. https://doi.org/10.1038/s41467-022-29222-7.
12. Song, C., Wang, Z., Yin, Z., Xiao, D., and Ma, D. (2022). Principles and applications of photothermal catalysis. Chem Catal. *2*, 52–83. https://doi.org/10.1016/j.checat.2021.10.005.
13. Geng, Z., Yu, Y., Offen, A.J., and Liu, J. (2023). Achieving maximum overall light enhancement in plasmonic catalysis by combining thermal and non-thermal effects. Nat. Catal. *6*, 1241–1247. https://doi.org/10.1038/s41929-023-01045-9.
14. Bai, X., Yuan, D., Li, Y., Song, H., Lu, Y., San, X., Lu, J., Fu, G., Wang, S., and Ye, J. (2021). Ambient sunlight-driven photothermal methanol dehydrogenation for syngas production with 32.9% solar-to-hydrogen conversion efficiency. iScience *24*, 102056. https://doi.org/10.1016/j.isci.2021.102056.
15. Zhang, J., Li, M., Tan, X., Shi, L., Xie, K., Zhao, X., Wang, S., Zhao, S., Zhang, H., Duan, X., et al. (2023). Confined FeNi alloy nanoparticles in carbon nanotubes for photothermal oxidative dehydrogenation of ethane by carbon dioxide. Appl. Catal., B *339*, 123166. https://doi.org/10.1016/j.apcatb.2023.123166.
16. Zhang, J., Xie, K., Jiang, Y., Li, M., Tan, X., Yang, Y., Zhao, X., Wang, L., Wang, Y., Wang, X., et al. (2023). Photoinducing different mechanisms on a Co-Ni bimetallic alloy in catalytic dry reforming of methane. ACS Catal. *13*, 10855–10865. https://doi.org/10.1021/acscatal.3c02525.
17. Cai, M., Li, C., An, X., Zhong, B., Zhou, Y., Feng, K., Wang, S., Zhang, C., Xiao, M., Wu, Z., et al. (2024). Supra-photothermal CO_2 methanation over greenhouse-like plasmonic superstructures of ultrasmall cobalt nanoparticles. Adv. Mater. *36*, 2308859. https://doi.org/10.1002/adma.202308859.
18. Zhu, Z., Tang, R., Li, C., An, X., and He, L. (2023). Promises of plasmonic antenna-reactor systems in gas-phase CO_2 photocatalysis. Adv. Sci. *10*, 2302568. https://doi.org/10.1002/advs.202302568.
19. Wu, Z., Shen, J., Li, C., Zhang, C., Wu, C., Li, Z., An, X., and He, L. (2023). Niche applications of mxene materials in photothermal catalysis. Chemistry *5*, 492–510. https://doi.org/10.3390/chemistry5010036.
20. Liu, X., He, F., Lu, Y., Wang, S., Zhao, C., Wang, S., Duan, X., Zhang, H., Zhao, X., Sun, H., et al. (2023). The double-edged effect of single atom metals on photocatalysis. Chem. Eng. J. *453*, 139833. https://doi.org/10.1016/j.cej.2022.139833.
21. Ghoussoub, M., Xia, M., Duchesne, P.N., Segal, D., and Ozin, G. (2019). Principles of photothermal gas-phase heterogeneous CO_2 catalysis. Energy Environ. Sci. *12*, 1122–1142. https://doi.org/10.1039/c8ee02790k.
22. Zhu, L., Gao, M., Peh, C.K.N., and Ho, G.W. (2018). Solar-driven photothermal nanostructured materials designs and prerequisites for evaporation and catalysis applications. Mater. Horiz. *5*, 323–343. https://doi.org/10.1039/c7mh01064h.
23. Meng, X., Wang, T., Liu, L., Ouyang, S., Li, P., Hu, H., Kako, T., Iwai, H., Tanaka, A., and Ye, J. (2014). Photothermal conversion of CO_2 into CH_4 with H_2 over group VIII nanocatalysts: An alternative approach for solar fuel production. Angew. Chem. Int. Ed. *53*, 11478–11482. https://doi.org/10.1002/anie.201404953.
24. Li, W., Zhang, Y., Wang, Y., Ran, W., Guan, Q., Yi, W., Zhang, L., Zhang, D., Li, N., and Yan, T. (2024). Graphdiyne facilitates photocatalytic CO_2 hydrogenation into C2+ hydrocarbons. Appl. Catal., B *340*, 123267. https://doi.org/10.1016/j.apcatb.2023.123267.

25. Wu, Z., Li, C., Li, Z., Feng, K., Cai, M., Zhang, D., Wang, S., Chu, M., Zhang, C., Shen, J., et al. (2021). Niobium and titanium carbides (mxenes) as superior photothermal supports for CO_2 photocatalysis. ACS Nano *15*, 5696–5705. https://doi.org/10.1021/acsnano.1c00990.
26. Lv, C., Bai, X., Ning, S., Song, C., Guan, Q., Liu, B., Li, Y., and Ye, J. (2023). Nanostructured materials for photothermal carbon dioxide hydrogenation: Regulating solar utilization and catalytic performance. ACS Nano *17*, 1725–1738. https://doi.org/10.1021/acsnano.2c09025.
27. Zhang, J., Chen, H., Duan, X., Sun, H., and Wang, S. (2023). Photothermal catalysis: From fundamentals to practical applications. Mater. Today *68*, 234–253. https://doi.org/10.1016/j.mattod.2023.06.017.
28. Shen, X., Li, C., Wu, Z., Tang, R., Shen, J., Chu, M., Xu, A.B., Zhang, B., He, L., and Zhang, X. (2022). Rationally designed nanoarray catalysts for boosted photothermal CO_2 hydrogenation. Nanoscale *14*, 11568–11574. https://doi.org/10.1039/d2nr02680e.
29. Shen, J., Tang, R., Wu, Z., Wang, X., Chu, M., Cai, M., Zhang, C., Zhang, L., Yin, K., He, L., and Li, C. (2022). Integrated photothermal nanoreactors for efficient hydrogenation of CO_2. Trans. Tianjin Univ. *28*, 236–244. https://doi.org/10.1007/s12209-022-00333-y.
30. Zhang, D., Lv, K., Li, C., Fang, Y., Wang, S., Chen, Z., Wu, Z., Guan, W., Lou, D., Sun, W., et al. (2020). All-earth-abundant photothermal silicon platform for CO_2 catalysis with nearly 100% sunlight harvesting ability. Sol. RRL *5*, 2000387. https://doi.org/10.1002/solr.202000387.
31. Zhang, C.C., Wu, Z.Y., Shen, J.H., He, L., and Sun, W. (2024). Silicon nanostructure arrays: An emerging platform for photothermal CO_2 catalysis. Acta Phys. Chim. Sin. *40*, 202304004. https://doi.org/10.3866/pku.Whxb202304004.
32. Yao, X., Hu, X., Zhang, W., Gong, X., Wang, X., Pillai, S.C., Dionysiou, D.D., and Wang, D. (2020). Mie resonance in hollow nanoshells of ternary TiO_2-Au-CdS and enhanced photocatalytic hydrogen evolution. Appl. Catal., B *276*, 119153. https://doi.org/10.1016/j.apcatb.2020.119153.
33. Zhou, L., Tan, Y., Wang, J., Xu, W., Yuan, Y., Cai, W., Zhu, S., and Zhu, J. (2016). 3D self-assembly of aluminium nanoparticles for plasmon-enhanced solar desalination. Nat. Photonics *10*, 393–398. https://doi.org/10.1038/nphoton.2016.75.
34. Cai, M.J., Li, C.R., and He, L. (2020). Enhancing photothermal CO_2 catalysis by thermal insulating substrates. Rare Met. *39*, 881–886. https://doi.org/10.1007/s12598-020-01431-3.
35. Li, Y., Bai, X., Yuan, D., Zhang, F., Li, B., San, X., Liang, B., Wang, S., Luo, J., and Fu, G. (2022). General heterostructure strategy of photothermal materials for scalable solar-heating hydrogen production without the consumption of artificial energy. Nat. Commun. *13*, 776. https://doi.org/10.1038/s41467-022-28364-y.
36. Cai, M., Wu, Z., Li, Z., Wang, L., Sun, W., Tountas, A.A., Li, C., Wang, S., Feng, K., Xu, A.B., et al. (2021). Greenhouse-inspired supra-photothermal CO_2 catalysis. Nat. Energy *6*, 807–814. https://doi.org/10.1038/s41560-021-00867-w.
37. Chiritescu, C., Cahill, D.G., Nguyen, N., Johnson, D., Bodapati, A., Keblinski, P., and Zschack, P. (2007). Ultralow thermal conductivity in disordered, layered WSe_2 crystals. Science *315*, 351–353. https://doi.org/10.1126/science.1136494.
38. Mavrokefalos, A., Nguyen, N.T., Pettes, M.T., Johnson, D.C., and Shi, L. (2007). In-plane thermal conductivity of disordered layered WSe_2 and $(W)_x(WSe_2)_y$ superlattice films. Appl. Phys. Lett. *91*. https://doi.org/10.1063/1.2800888.
39. Rupprechter, G. (2021). Operando surface spectroscopy and microscopy during catalytic reactions: From clusters via nanoparticles to meso-scale aggregates. Small *17*, e2004289. https://doi.org/10.1002/smll.202004289.
40. Dong, C., Lian, C., Hu, S., Deng, Z., Gong, J., Li, M., Liu, H., Xing, M., and Zhang, J. (2018). Size-dependent activity and selectivity of carbon dioxide photocatalytic reduction over platinum nanoparticles. Nat. Commun. *9*, 1252. https://doi.org/10.1038/s41467-018-03666-2.
41. Dong, C., Li, Y., Cheng, D., Zhang, M., Liu, J., Wang, Y.-G., Xiao, D., and Ma, D. (2020). Supported metal clusters: Fabrication and application in heterogeneous catalysis. ACS Catal. *10*, 11011–11045. https://doi.org/10.1021/acscatal.0c02818.
42. Kong, N., Han, B., Li, Z., Fang, Y., Feng, K., Wu, Z., Wang, S., Xu, A.-B., Yu, Y., Li, C., et al. (2020). Ruthenium nanoparticles supported on $Mg(OH)_2$ microflowers as catalysts for photothermal carbon dioxide hydrogenation. ACS Appl. Nano Mater. *3*, 3028–3033. https://doi.org/10.1021/acsanm.0c00383.
43. Wu, Z., Shen, J., Li, C., Zhang, C., Feng, K., Wang, Z., Wang, X., Meira, D.M., Cai, M., Zhang, D., et al. (2022). Mo_2TiC_2 mxene-supported ru clusters for efficient photothermal reverse water-gas shift. ACS Nano *17*, 1550–1559. https://doi.org/10.1021/acsnano.2c10707.
44. Han, B., Lin, Y., Yang, Y., Mao, N., Li, W., Wang, H., Yasuda, K., Wang, X., Fatemi, V., Zhou, L., et al. (2020). Deep-learning-enabled fast optical identification and characterization of 2D Materials. Adv. Mater. *32*, 2000953. https://doi.org/10.1002/adma.202000953.
45. Chuang, H.-J., Tan, X., Ghimire, N.J., Perera, M.M., Chamlagain, B., Cheng, M.M.-C., Yan, J., Mandrus, D., Tománek, D., and Zhou, Z. (2014). High mobility WSe_2 p- and n-type field-effect transistors contacted by highly doped graphene for low-resistance contacts. Nano Lett. *14*, 3594–3601. https://doi.org/10.1021/nl501275p.
46. Wang, Q.H., Kalantar-Zadeh, K., Kis, A., Coleman, J.N., and Strano, M.S. (2012). Electronics and optoelectronics of two-dimensional transition metal dichalcogenides. Nat. Nanotechnol. *7*, 699–712. https://doi.org/10.1038/nnano.2012.193.
47. Luo, Y., Yu, L., Men, J., Feng, J., Jiang, Y., Li, L., Qin, G., and Feng, J. (2023). Ultralow thermal conductivity of single-atom doped carbon aerogel synthesized with a facile ambient-pressure-drying strategy. Carbon *213*, 118167. https://doi.org/10.1016/j.carbon.2023.118167.
48. Liu, Z., Zhao, H., Li, N., Zhang, Y., Zhang, X., and Du, Y. (2016). Assembled 3D electrocatalysts for efficient hydrogen evolution: WSe_2 layers anchored on graphene sheets. Inorg. Chem. Front. *3*, 313–319. https://doi.org/10.1039/C5QI00216H.
49. Li, H., Lu, G., Wang, Y., Yin, Z., Cong, C., He, Q., Wang, L., Ding, F., Yu, T., and Zhang, H. (2013). Mechanical exfoliation and characterization of single- and few-layer nanosheets of WSe_2, TaS_2, and $TaSe_2$. Small *9*, 1974–1981. https://doi.org/10.1002/smll.201202919.
50. Zhou, J., Li, J., Kan, L., Zhang, L., Huang, Q., Yan, Y., Chen, Y., Liu, J., Li, S.-L., and Lan, Y.-Q. (2022). Linking oxidative and reductive clusters to prepare crystalline porous catalysts for photocatalytic CO_2 reduction with H_2O. Nat. Commun. *13*, 4681. https://doi.org/10.1038/s41467-022-32449-z.
51. Shi, J., Li, H., Genest, A., Zhao, W., Qi, P., Wang, T., and Rupprechter, G. (2022). High-performance water gas shift induced by asymmetric oxygen vacancies: Gold clusters supported by ceria-praseodymia mixed oxides. Appl. Catal., B *301*, 120789. https://doi.org/10.1016/j.apcatb.2021.120789.
52. Yao, S., Lin, L., Liao, W., Rui, N., Li, N., Liu, Z., Cen, J., Zhang, F., Li, X., Song, L., et al. (2019). Exploring metal–support interactions to immobilize subnanometer Co clusters on γ–Mo_2N: A highly selective and stable catalyst for CO_2 activation. ACS Catal. *9*, 9087–9097. https://doi.org/10.1021/acscatal.9b01945.
53. Zhang, X., Zhang, M., Deng, Y., Xu, M., Artiglia, L., Wen, W., Gao, R., Chen, B., Yao, S., Zhang, X., et al. (2021). A stable low-temperature H_2-production catalyst by crowding Pt on α-MoC. Nature *589*, 396–401. https://doi.org/10.1038/s41586-020-03130-6.
54. Kou, J., Wang, W.D., Fang, J., Li, F., Zhao, H., Li, J., Zhu, H., Li, B., and Dong, Z. (2022). Precisely controlled Pd nanoclusters confined in porous organic cages for size-dependent catalytic hydrogenation. Appl. Catal., B *315*, 121487. https://doi.org/10.1016/j.apcatb.2022.121487.
55. Wang, L., Liu, H., Zhuang, J., and Wang, D. (2022). Small-scale big science: From nano- to atomically dispersed catalytic materials. Small Sci. *2*, 2200036. https://doi.org/10.1002/smsc.202200036.
56. Kaneva, M.V., Reveguk, A.A., and Tolstoy, V.P. (2022). SILD-preparation of nanostructured Ru_x^0-RuO_2●nH_2O thin films: Effect of deposition cycles on electrocatalytic properties. Ceram. Int. *48*, 11672–11677. https://doi.org/10.1016/j.ceramint.2022.01.025.
57. Tang, R., Zhu, Z., Li, C., Xiao, M., Wu, Z., Zhang, D., Zhang, C., Xiao, Y., Chu, M., Genest, A., et al. (2021). Ru-catalyzed reverse water gas shift reaction with near-unity selectivity and superior stability. ACS Mater. Lett. *3*, 1652–1659. https://doi.org/10.1021/acsmaterialslett.1c00523.
58. Zhou, Y., Xie, Z., Jiang, J., Wang, J., Song, X., He, Q., Ding, W., and Wei, Z. (2020). Lattice-confined Ru clusters with high CO tolerance and activity for the hydrogen oxidation reaction. Nat. Catal. *3*, 454–462. https://doi.org/10.1038/s41929-020-0446-9.
59. Hoch, L.B., O'Brien, P.G., Jelle, A., Sandhel, A., Perovic, D.D., Mims, C.A., and Ozin, G.A. (2016). Nanostructured indium oxide coated silicon nanowire arrays: A hybrid photothermal/photochemical approach to solar fuels. ACS Nano *10*, 9017–9025. https://doi.org/10.1021/acsnano.6b05416.
60. Wang, Z., Liu, Y., Huang, B., Dai, Y., Lou, Z., Wang, G., Zhang, X., and Qin, X. (2014). Progress on extending the light absorption

spectra of photocatalysts. Phys. Chem. Chem. Phys. *16*, 2758–2774. https://doi.org/10.1039/C3CP53817F.

61. Joya, K.S., and de Groot, H.J.M. (2013). Electrochemical *in situ* surface enhanced Raman spectroscopic characterization of a trinuclear ruthenium complex, Ru-red. J. Raman Spectrosc. *44*, 1195–1199. https://doi.org/10.1002/jrs.4329.
62. Zhu, R.J., Kang, L.L., Li, L., Pan, X.L., Wang, H., Su, Y., Li, G.Y., Cheng, H.K., Li, R.G., Liu, X.Y., and Wang, A.Q. (2024). Photo-thermo catalytic oxidation of C_3H_8 and C_3H_6 over the WO_3-TiO_2 supported pt single-atom catalyst. Acta Phys. Chim. Sin. *40*, 2303003. https://doi.org/10.3866/pku.Whxb202303003.
63. Tebar-Soler, C., Martin-Diaconescu, V., Simonelli, L., Missyul, A., Perez-Dieste, V., Villar-Garcia, I.J., Brubach, J.B., Roy, P., Haro, M.L., Calvino, J.J., et al. (2023). Low-oxidation-state Ru sites stabilized in carbon-doped RuO_2 with low-temperature CO_2 activation to yield methane. Nat. Mater. *22*, 762–768. https://doi.org/10.1038/s41563-023-01540-1.
64. Zhao, Y., Cong, H., Li, P., Wu, D., Chen, S., and Luo, W. (2021). Hexagonal $RuSe_2$ nanosheets for highly efficient hydrogen evolution electrocatalysis. Angew. Chem. Int. Ed. *60*, 7013–7017. https://doi.org/10.1002/anie.202016207.
65. Zhang, X., Zhu, X., Lin, L., Yao, S., Zhang, M., Liu, X., Wang, X., Li, Y.W., Shi, C., and Ma, D. (2017). Highly dispersed copper over β-Mo_2C as an efficient and stable catalyst for the reverse water gas shift (RWGS) reaction. ACS Catal. *7*, 912–918. https://doi.org/10.1021/acscatal.6b02991.

STAR★METHODS

KEY RESOURCES TABLE

REAGENT or RESOURCE	SOURCE	IDENTIFIER
Chemicals, peptides, and recombinant proteins		
Selenium (≥99.99%, metals basis)	Macklin	CAS: 7782-49-2
Sodium borohydride (99%)	Thermo scientific	CAS: 200050250
N, N-Dimethylformamide (for GC-HS, ≥99.9%)	Aladdin	CAS: 68-12-2
Sodium tungstate dihydrate (99%)	Energy chemical	CAS: 10213-10-2
Carbon disulfide (GC, ≥99.5%)	Aladdin	CAS: 75-15-0
Sodium hydroxide (ACS, 97%)	Aladdin	CAS: 1310-73-2
Silicon dioxide (catalyst support, High surface area)	Alfa Aesar	CAS: 44740
Ruthenium (III) trichloride anhydrous	Aladdin	CAS: 10049-08-8

RESOURCE AVAILABILITY

Lead contact

Further information and requests for resources should be directed to and will be fulfilled by the lead contact, Le He (lehe@suda.edu.cn).

Materials availability

All materials generated in this study are available from the lead contact without restriction.

Data and code availability

- The datasets and images generated during this study are available from the lead contact upon request.
- This paper does not report original code.
- Any additional information required to reanalyze the data reported in this paper is available from the lead contact upon request.

METHOD DETAILS

Materials

All the chemicals purchased were used without further purification. Selenium (Se) was purchased from Macklin. N, N-Dimethylformamide (DMF), Carbon disulfide (CS_2), Sodium hydroxide (NaOH), and Ruthenium (III) trichloride anhydrous ($RuCl_3$) were purchased from Aladdin. Sodium borohydride ($NaBH_4$) was purchased from Thermo scientific. Sodium tungstate dihydrate ($Na_2WO_4 \cdot 2H_2O$) was purchased from Energy chemical. Silicon dioxide (SiO_2, catalyst support, High surface area) was purchased from Alfa Aesar.

Synthesis of WSe_2 powders

0.632 g of Se powder and 0.189 g of $NaBH_4$ were dissolved in 60 mL DMF and stirred vigorously for 2 h. Then $Na_2WO_4 \cdot 2H_2O$ (1.319 g) was added into solution and stirred for another 30 min. After that, the solution was transferred to an 80 mL Teflon-lined stainless-steel autoclave and heated in the oven at 240°C for 48 h. The precipitate was obtained from the solution in the autoclave through centrifugation. Firstly, it was washed several times with CS_2 and NaOH solution to remove any unreacted reactants, and then with DI water and ethanol. After drying in a vacuum oven, the black power was finally annealed at 300°C for 5 h under Ar atmosphere.

Synthesis of Ru/SiO_2 catalysts

We prepared the Ru/SiO_2 catalyst using a traditional impregnation method with SiO_2 as the support. The process involved dissolving 200 mg of ground silica powder in 5 mL of ethanol and sonication for 30 min. 2 mg of $RuCl_3$ dissolved in 2 mL of ethanol was added to the ethanol solution, followed by evaporation at 90°C under vigorously stirring. The resulting powder was calcined at 200°C for 2 h in air with a heating rate of 5°C/min. The Ru/SiO_2 powders were finally obtained after being calcined at 200°C for 2 h in H_2 with a heating rate of 5°C/min.

Characterizations

X-ray diffraction (XRD) was performed on a Bruker D2-Phaser X-ray diffractometer with Cu Ka radiation. Transmission electron microscopy (TEM) images were obtained with an FEI-Tecnai F20TEM. Scanning electron microscopy (SEM) images were acquired on a Zeiss G500

instrument. The data of diffuse reflectance spectra (DRS) were collected using a Lambda 950 ultraviolet-vis-near infrared (UV-vis-NIR) spectrometer from PerkinElmer with a spectrum ranging from 250 nm to 2500 nm. Infrared images were obtained with a Fotric 320Q camera. Raman tests were tested with a Renishaw *in situ* Raman test system (inVia Qontor). During the *in situ* Raman measurements, a 785 nm Raman laser was used with external illumination at 1 sun or 3 suns by a Xe lamp. An accumulation time of 10 s and laser power of 5% were used in the measurement of each spectrum. During Raman measurements, external illumination was first performed on the samples for different amount of times (10s, 15s, 20s, and 30s) before it was switched off for laser exposure.

Photocatalytic testing

For gas-phase photocatalytic tests, the glass fiber substrates, Cu sheet, and Si slice were cut to 2.25 cm^2 to standardize the area of the substrate. The Cu sheet and Si slice were cleaned with ethanol and deionized water several times. Ru/SiO_2 samples were prepared by drop-casting ~5 mg Ru/SiO_2 powders from ethanol dispersion and dried in an oven at 50°C for 12 h. For the Ru/SiO_2-WSe_2 sample, the preparation was divided into two main steps. Firstly, different masses of WSe_2 powders (5 mg, 10 mg, and 15 mg) were dispersed in ethanol under sonication. The suspension was transferred onto a substrate by drop-casting, followed by drying the catalyst film in a vacuum oven. Second, 5 mg of Ru/SiO_2 powders were dispersed in ethanol and transferred on top of the WSe_2-substrate structure by drop-casting.

The gas-phase photothermal CO_2 reduction rate was measured in a transparent glass batch reactor with an annular sealed glass cover. After vacuum pumping the reaction system, a mixture of CO_2 and H_2 (1:1) was introduced into the reactor to reach ~100 kPa, and the reaction was monitored using an MIK-P300 pressure transducer. The photothermal CO_2 conversion was driven by a 300 W Xenon arc lamp with a 2.25 cm^2 sample located in the center of the reactor. The power intensity of light was measured using a Spectra-Physics power meter to be 2.9 W/cm^2 without any filters. The contents of product gases (CO and CH_4) in the reaction system were measured by gas chromatography (GC7900, Techcomp) with a flame ionization detector (FID) connected to a catalytic converter. The reaction time was set to be 10 min.

The CO_2 conversion rate (R_{co_2}), seen as characteristic of the photothermal catalytic activity, was defined as the sum of the CO formation rate (F_{CO}) and CH_4 formation rate (F_{CH_4}). F_{CO} and F_{CH_4} are defined as

$$F_{CO} = \frac{n_{CO}}{m_{cat}\omega_{Ru}t}$$

$$F_{CH_4} = \frac{n_{CH_4}}{m_{cat}\omega_{Ru}t}$$

$$R_{co_2} = F_{CO} + F_{CH_4}$$

and the selectivity of CO is defined as

$$S_{CO} = \frac{F_{CO}}{F_{CO}+F_{CH_4}}$$

where n is the yield of products (units of mol), ω_{Ru} is the loading percent of Ru, m_{cat} is the mass of the catalyst (units of g) and t is the irradiation time (units of hour).